

that the potential on the capacitor whose gap has misfired may reach a maximum reversed potential approaching 2.6 times the initial potential to which it is charged.

The five-stage cascade charging circuit consists of five banks of seven 7.5- μ f pyranol capacitors of 20-kv rating that are charged in parallel and discharged in series through a 50- μ h inductance from which ten RG-17/U cables 10 m long lead to the individual 100-kv capacitors. Five four-element spark gap switches carry out the switching operation. The 100-kv capacitors are charged in 50 μ sec to the potential 5.25 V_c , where V_c is the potential to which the cascade bank is charged. The capacitors in this bank are found to have a long life since they do not oscillate in potential. The charging inductor serves to isolate the cascade bank from the

oscillating potential of the 100-kv capacitors during the operation of Scylla.

Note added in proof.—Reference to the work on axial magnetic field compression devices would not be complete without mention of recent work at the General Electric Research Laboratory²⁸ as well as that in Aachen, Germany,²⁹ in Fontenay-aux-Roses, France,³⁰ in Rome, Italy,³¹ and in Sukhumi, U.S.S.R.³²

²⁸ H. C. Pollock, L. M. Goldman, and F. Westendorp, *Bull. Am. Phys. Soc.* **5**, 367 (1960).

²⁹ H. Fay, E. Hintz, and H. L. Jordan, *4th International Conference on Ionization Phenomena in Gases, Uppsala, Sweden* (North-Holland Publishing Company, Amsterdam, 1960).

³⁰ M. Alidieres, R. Aymar, C. Etievant, P. Jourdan, P. Langer, and A. Samain, see footnote 29.

³¹ J. E. Allen and S. Segre, see footnote 29.

³² I. F. Kwartshava, K. N. Kervalidze, and J. S. Gvaladze, see footnote 29.

Continuum Radiation in the X Ray and Visible Regions from a Magnetically Compressed Plasma (Scylla)*

F. C. JAHODA, E. M. LITTLE, W. E. QUINN, G. A. SAWYER, AND T. F. STRATTON
Los Alamos Scientific Laboratory, University of California, Los Alamos, New Mexico

(Received March 28, 1960)

The identification of a sharp low-wavelength cutoff in the spectrum of x rays emitted from deuterium discharges in Scylla has resulted in the assignment of an electron temperature of 240 ± 40 ev at the time of peak magnetic field compression. Simultaneous time-resolved absolute intensity determinations in the visible continuum, when coupled with the temperature measurement, yield an upper limit electron number density of $(5 \pm 1) \times 10^{16}/\text{cm}^3$ at peak compression. The absolute value of $dE/d\lambda$ in the soft x ray region is two hundred times larger than bremsstrahlung from a pure deuterium plasma at the temperature and density quoted, and it is postulated that the large experimental $dE/d\lambda$ is the result of recombination radiation from about 2% of oxygen contaminant from the discharge tube walls.

I. INTRODUCTION

IT is possible, in principle, to determine many of the properties and characteristics of a plasma from an examination of the electromagnetic radiation emitted from the plasma itself. In particular, if the plasma temperature is greater than about 100 ev, the most characteristic radiation from pure deuterium is bremsstrahlung from electrons accelerated in the Coulomb field of the ions, and the electron temperature and density can be estimated from the spectrum shape and the total radiated power. If impurities are present, recombination and line radiation obscures the free-free radiation, particularly near the shorter wavelengths, and an interpretation of the experiment must be modified to include these processes. Spectral lines, where present, can be analyzed in terms of thermal or pressure broadening to yield information about the temperature and density, respectively. These techniques have been applied to the Scylla plasma compression

experiment to measure the temperature, density, and purity of the deuterium discharge.

The Scylla experiment has been described previously.¹⁻³ In addition, detailed descriptions of other aspects of the apparatus and experimental results are presented in the articles preceding and following this account.^{4,5} The data reported there show that the magnetic field compressing the plasma reaches 50 kilogauss in 1.25 μ sec, and that about 3 cm^3 of volume is raised to a number density approaching $10^{17}/\text{cm}^3$ and a deuteron temperature of 1.3 kev. In addition, at the time of neutron emission, soft x rays are detected

¹ W. C. Elmore, E. M. Little, and W. E. Quinn, *Phys. Rev. Letters* **1**, 32 (1958).

² W. C. Elmore, E. M. Little, and W. E. Quinn, (with K. Boyer), *Proceedings of the Second United Nations International Conference on the Peaceful Uses of Atomic Energy, Geneva, 1958* (United Nations, Geneva, 1958), Vol. 32, p. 337.

³ D. E. Nagle, W. E. Quinn, W. B. Riesenfeld, and W. Leland, *Phys. Rev. Letters* **3**, 318 (1959).

⁴ K. Boyer, W. C. Elmore, E. M. Little, W. E. Quinn, and J. L. Tuck, preceding paper [*Phys. Rev.* **119**, 831 (1960)].

⁵ D. E. Nagle, W. E. Quinn, F. L. Ribe, and W. B. Riesenfeld, following paper [*Phys. Rev.* **119**, 857 (1960)].

* Work performed under the auspices of the U. S. Atomic Energy Commission.

which have an energy of about one keV and are produced in the gas.^{6,7}

The analysis reported here of the x-ray spectrum, as well as the associated visible continuum, shows that the electron temperature is less than the ion temperature and that the electron density is in agreement with the observed geometrical compression and also with the deuteron density inferred from the measured nuclear reaction rate, deuteron temperature, and volume of neutron emitting plasma.

A preliminary report on some sections of this work was given at Uppsala, and appeared in the published proceedings of the conference.⁸

II. FREE-FREE AND FREE-BOUND CONTINUUM RADIATION

The bremsstrahlung emission per unit frequency interval and unit volume for N_e electrons per unit volume with temperature T_e resulting from the interaction with N_i ions per unit volume of effective nuclear charge Z is⁹:

$$E_\nu = CN_e N_i Z^2 (\chi_H/kT_e)^{3/2} \bar{g} e^{-h\nu/kT_e}, \quad (1)$$

where

$$C = 2^7 (\pi/3)^{3/2} \alpha^3 \chi_H a_0^3 = 1.7 \times 10^{-40} \text{ erg-cm}^3.$$

α is the fine structure constant, a_0 is the Bohr radius, and χ_H is the hydrogen ionization potential. \bar{g} is the Gaunt factor, which represents the departure of the quantum-mechanical calculation from the classical result, averaged over the Maxwell velocity distribution at electron temperature T_e . The Gaunt factor for an unscreened Coulomb potential has been evaluated numerically by Karzas and Latter¹⁰ and is an important correction in the visible wavelength region for the high temperatures considered here. Converting to emission per unit wavelength,

$$E_\lambda = 1.9 \times 10^{-28} N_e N_i Z^2 \bar{g} (kT_e)^{-3/2} \lambda^{-2} e^{-12395/\lambda kT_e} \text{ watts/cm}^2\text{-angstrom}. \quad (2)$$

The total radiation power for a hydrogen plasma, obtained by integrating over all wavelengths, is:

$$\int_0^\infty E_\lambda d\lambda = 1.5 \times 10^{-32} (kT_e)^{3/2} \bar{g}_1 N_e N_i \text{ watts/cm}^3. \quad (3)$$

In Eqs. (2) and (3), kT_e is in eV, and λ is in angstroms. Figure 1 shows the classical bremsstrahlung energy spectra, i.e., $\bar{g}=1$, in the wavelength range of 1 to 100 angstroms for temperatures of 0.2 to 1.0 keV. The

⁶ K. Boyer, E. M. Little, W. E. Quinn, G. A. Sawyer, and T. F. Stratton, *Phys. Rev. Letters* **2**, 279 (1958).

⁷ H. R. Griem, A. C. Kolb, and W. R. Faust, *Phys. Rev. Letters* **2**, 281 (1958).

⁸ F. L. Ribe, *Proceedings of the Fourth International Conference on Ionization Phenomena in Gases, Uppsala* (North-Holland Publishing Company, Amsterdam, 1960).

⁹ G. Elwert, *Z. Naturforsch.* **9a**, 637 (1954).

¹⁰ W. J. Karzas and R. Latter, The Rand Corporation Report AECU-3703, rev., 1958 (unpublished).

spectra peak between 5 and 15 angstroms, and an appreciable fraction of the total emission is in the soft x-ray region. The strong exponential dependence of the spectrum in the neighborhood of the short wavelength cutoff implies that the most sensitive temperature measurement can be made in the x-ray region, whereas the density is most readily measured in the visible, where the temperature dependence reduces to $T_e^{-3/2}$.

If impurity ions are present, there will also be free-bound (recombination) and bound-bound (line) radiation from the impurities. The recombination emission per unit frequency interval per impurity ion of charge $i+1$ for N_e electrons per unit volume with temperature T_e is⁹:

$$\frac{E_\nu}{N_{i+1}} = \sum_n C N_e \left(\frac{\chi_H}{kT_e} \right)^{3/2} \left(\frac{\chi_n}{\chi_H} \right)^{2\xi_n} \frac{f_1}{n} e^{(\chi_n - h\nu)/kT_e}, \quad (4)$$

where C is as before, $\chi_n = h\nu_n$ is the ionization potential from the n th shell of the ion of charge i , n is the principal quantum number of the final state, ξ_n is the number of empty places in the n th shell, and f_1 is the free-bound Gaunt correction.¹¹ Aside from small effects due to the Gaunt factor, recombination radiation has the same spectral shape as free-free radiation except for the fact that there are low-frequency cutoffs when the energy of the emitted quantum equals an ionization energy of the emitting ion, that is, when a zero energy electron falls into the n th shell. Because of the factor $n^{-1}(\chi_n/\chi_H)^2 e^{\chi_n/kT_e}$, ion species with large ionization potentials and low quantum numbers are particularly effective sources of free-bound radiation.

Impurity line radiation is much more difficult to express in closed form, but Knorr¹² estimates that even for such a low Z impurity as oxygen, the electron temperature must approach one keV before the total line radiation becomes less important than recombination radiation. These estimates are based on the assumptions that the plasma dimensions are so small that the optical thickness is negligible and that the density is

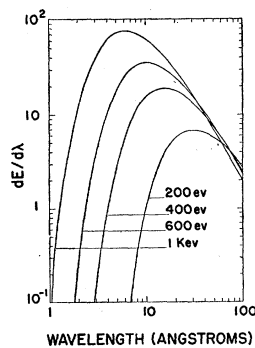


FIG. 1. Bremsstrahlung spectra as a function of electron temperature. The curves are to the same scale but the ordinate is in arbitrary units.

¹¹ W. J. Karzas and R. Latter, The Rand Corporation Report RM-2091-AEC, 1958 (unpublished).

¹² G. Knorr, *Z. Naturforsch.* **13a**, 941 (1958).

low enough to allow all excited states to fall radiatively to the ground state before any further electron excitation occurs.

III. X-RAY MEASUREMENTS

Experimental Apparatus

Figure 2 is a drawing of the geometry for the experiments in the soft x-ray region. A pinhole aperture one mm in diameter 60 cm from the midplane of the driving coil limited the solid angle to 2.2×10^{-6} steradian. With the pinhole 60 cm from the midplane of the discharge, there was no clogging of the aperture with discharge tube debris and the solid angle remained constant with time. In order to eliminate the possibility of fast electrons passing through the pinhole and producing a signal in the detector, a magnetron magnet with a field strength of 1000 gauss was placed so that its field was across the pinhole. 20 cm behind the pinhole was the detector, which consisted either of an x-ray sensitive photographic emulsion or a scintillator material mounted on the face of a 6810A photomultiplier tube. The photomultiplier tube was protected from the stray magnetic field of the electron deflecting magnet by five 0.005-in. thick sleeves of high permeability iron, and was screened from the strong leakage pulsed magnetic field of the driving coil by a 2 mm thick brass cylinder enclosing the detector assembly. Electrostatic pickup in the photomultiplier was eliminated by enclosing the entire detector and the coaxial voltage and signal leads in copper tubing leading to a shielded room containing the oscilloscope and photomultiplier high-voltage power supply. Because the discharge becomes contaminated with wall materials after the first ten μsec , it was necessary to protect the detector from the intense visible light emitted at late times in the discharge cycle by placing a thin metal foil in front of the photographic film or scintillator material. Foil holders which were mounted interchangeably on the front of the photomultiplier assembly formed a field stop to limit the region viewed by the detector to a diameter of two centimeters at the

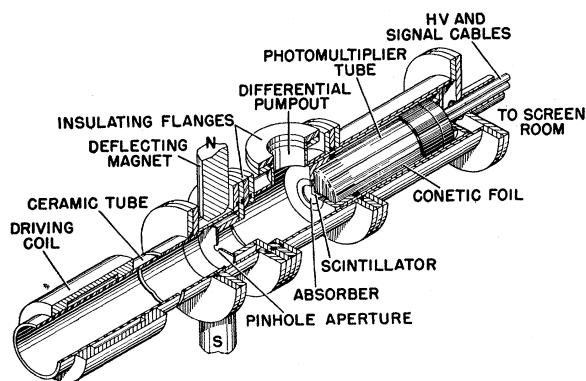


FIG. 2. Apparatus for observing soft x rays. The ceramic discharge tube is 5.1-cm inside diameter.

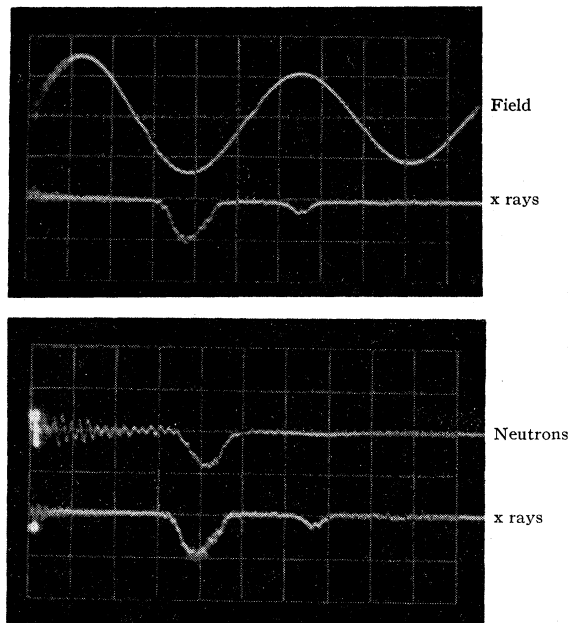


FIG. 3. X-ray and neutron correlation with the driving magnetic field. One large division of the oscilloscope grid is $1 \mu\text{sec}$. The two oscillograms were recorded for the same discharge.

midplane of the coil. In addition to excluding visible light, the foils prevented low-energy neutral or ionized atoms from reaching the detector. The volume between the pinhole and the detector was differentially pumped to a pressure of about 10^{-3} mm Hg.

The time dependence of the x-radiation was established by displaying the signal produced by the scintillator and photomultiplier directly on a Tektronix Model 551 dual-beam oscilloscope. Figure 3 shows oscilloscope records of the driving-coil magnetic field, neutron emission, and x-ray emission. The scintillator was protected from visible light by 1.5 mg/cm^2 of aluminum. The signal cable was terminated in its characteristic impedance so that the voltage signal displayed by the oscilloscope was a faithful representation of the photomultiplier output current. It is apparent from the traces that neutrons and x rays are emitted during the peak compression of the second half-cycle of the magnetic field, and that the x rays are emitted at the same time as the neutrons. The precaution of making the plastic scintillator¹³ only 0.1 mm thick reduced the counter efficiency for hard x rays sometimes produced by acceleration of runaway electrons in the induction field. Neutrons and protons of about three Mev energy from the $d-d$ reaction were an additional possibility for the origin of the signal, but simple considerations of numbers and geometry in the case of protons, and detector efficiency in the case of neutrons, were sufficient to eliminate these particles as signal sources.

¹³ Pilot Scintillator B. Pilot Chemicals, Inc., Watertown, Massachusetts.

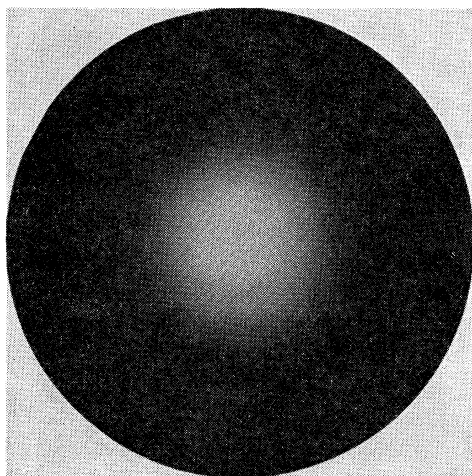


FIG. 4. Pinhole photograph of soft x rays emitted along the discharge tube axis. The circular boundary corresponds to the 5.1-cm inside diameter of the discharge tube at the mid-plane of the driving coil.

The area and location of the emission region was determined by replacing the scintillator and photomultiplier by a photographic emulsion to record a pinhole photograph of the discharge in soft x-ray light. The field stop was removed for these observations so that the entire discharge tube was imaged. A typical photograph obtained under these conditions is reproduced in Fig. 4. 1.5 mg/cm² aluminum protected the film from visible light, and the negative was masked in exposing the print so that the circular boundary of the picture corresponds to the inner wall of the ceramic discharge tube at the midplane of the driving coil. The photograph reveals that the x-ray emitting region is centered in the discharge tube, that its diameter is about 1.5 cm, and that there is no x-ray production at the tube wall.

The position of the x-ray emitting region in the tube depends on the way the coil is connected to the parallel plate transmission line. When the transmission line leaving the coil has the same width as the coil itself, the x-ray emission region is centered as shown in Fig. 4. However, if the transmission line is wider than the coil so that an abrupt change in width occurs at the feedpoint, the x-ray photographs show that the emitting region is displaced about 0.5 cm toward the feedpoint. This behavior can be easily understood in terms of magnetic field gradients, because when the width of the transmission line is greater than the width of the driving coil, the magnetic field in the coil is greater than the magnetic field between the plates of the line and the plasma is pushed toward the feedpoint.

Among all the characteristics of x radiation, the best known experimentally are the mass absorption coefficients as a function of wavelength and absorber material (Fig. 5). Measurement of the transmission of x rays through absorbers of various thicknesses and

materials is therefore a technique for the spectral analysis of the incident radiation.

Thin free foils of beryllium,¹⁴ polyethylene, aluminum, and nickel were used for the absorption measurements. The thinnest polyethylene and Ni samples were 0.5 mg/cm² thick while the thinnest Be and Al foils were 1.2 and 1.5 mg/cm², respectively. The foil thicknesses were determined by weighing a measured area of the material on an analytical balance, and were accurate to three percent. It was important to establish the purity of the materials, particularly with respect to high *Z* contaminants because the x-ray mass absorption coefficient is a strong function of atomic number. Spectrochemical analysis¹⁵ of the Be, Al, and Ni revealed no contaminant of sufficient concentration to require correction of the mass absorption coefficients. Combustion and infrared analysis¹⁶ of the polyethylene revealed that it was 99.5 percent CH₂, with oxygen as the principal impurity. Because the absorption coefficient of hydrogen is negligible compared to that of carbon, the CH₂ absorbers were treated as carbon of the appropriate density. They were rendered opaque to visible radiation by evaporating Al onto both sides of the CH₂ film to a total thickness of 50 μg/cm², and a correction to the CH₂ mass absorption coefficient was applied for the aluminum.

Absorption measurements yield information about the spectrum of incident x rays by the shape of the plot of transmitted intensity vs absorber thickness. In addition, if the signal can be referred to an absolute scale, information about the number density of the emitting plasma, and the presence, or absence, of impurity ions can be derived. For this purpose, both a NaI scintillation counter and an argon-filled ionization chamber were calibrated on an absolute energy scale. The NaI detector was calibrated by establishing the end points of the gamma-ray spectra of Co⁶⁰, Mn⁵⁴, Cs¹³⁷, and Am²⁴¹, which provide gamma-rays ranging in energy from 0.018 to 1.3 Mev. A straight line passing through these calibration points was extrapolated to

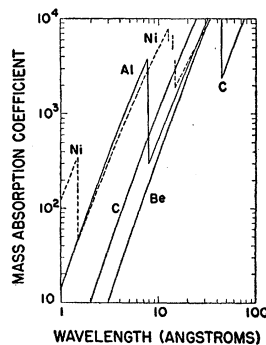


FIG. 5. Mass absorption coefficients for various absorbers. The *K* and *L* edges allow sensitive comparisons of experimental transmissions with calculated source characteristics.

¹⁴ Supplied by J. A. Northrup, Cyclotron Group, Los Alamos Scientific Laboratory.

¹⁵ Analyzed by Spectrochemical Analysis Group, Los Alamos Scientific Laboratory.

¹⁶ Analyzed by R. Rogers, Group GMX-2, Los Alamos Scientific Laboratory.

the origin. For the calibration, the pulse height from the gamma-ray was integrated by a simple RC network so that the total charge produced in the scintillation counter for a given deposited energy in the crystal was obtained. The RC time constant was sufficiently long ($10 \mu\text{sec}$) to integrate the x-ray pulse from Scylla ($0.8 \mu\text{sec}$ half-width) without appreciable correction. Since a typical x-ray signal on the detector corresponded to 10^{-2} erg ($\sim 10^{10}$ ev) it was necessary to adjust the gain of the detector with the photomultiplier voltage, so that in combination with the oscilloscope amplifier sensitivity, a total dynamic range of about 10^6 was obtained. The photomultiplier gain as a function of voltage was measured by examining the pulse produced in the multiplier by a xenon flash lamp, as a function of distance and photomultiplier voltage. Because the energy from a single gamma ray was deposited in the NaI in an infinitesimal time compared to the $0.8\text{-}\mu\text{sec}$ x-ray pulse from Scylla, there was the possibility of calibration error because of the time response of the electronics. To eliminate this possibility, a betatron x-ray source¹⁷ with a pulse shape similar to the Scylla x-ray pulse provided calibrations for finite pulse widths.

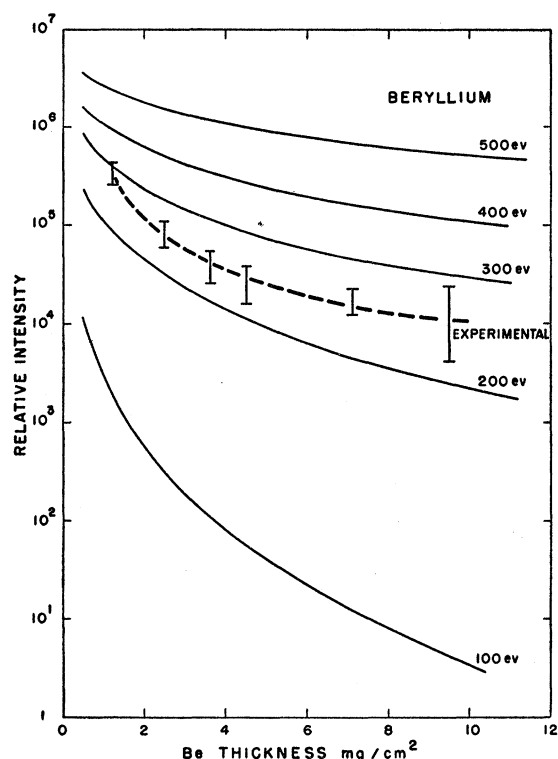


FIG. 6. Experimental beryllium absorption curve compared with calculated transmissions for bremsstrahlung spectra from different temperature sources. The experimental data correspond in time to the peak magnetic field compression.

¹⁷ R. R. Stevens, Group GMX-11, Los Alamos Scientific Laboratory, operated the betatron and supplied us with the spectral and calibration data.

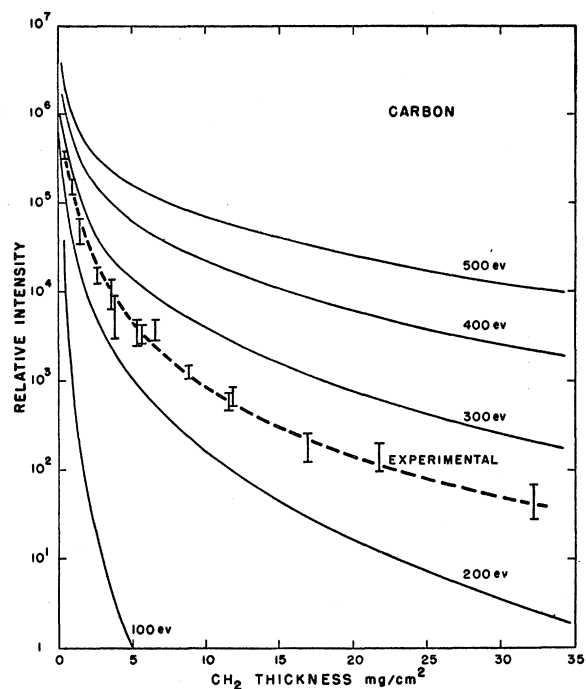


FIG. 7. Experimental polyethylene absorption curve compared with calculated transmissions. The carbon transmission has been corrected for the thin evaporated aluminum films necessary to exclude visible light and for the hydrogen fraction of polyethylene.

The betatron and the radioactive source calibrations agreed within 20%.

The response of scintillation crystals to very low-energy quanta has not been experimentally determined, and those experiments that are available indicate nonlinearities below 100 keV.¹⁸ Ionization chambers, on the other hand, are known to be linear from 300 keV to 300 eV for electrons as primaries.¹⁹ In addition, absolute values for the energy required to produce a single ion pair are well known experimentally. Accordingly, a parallel plate, argon filled, ionization chamber was constructed to supplement the absolute intensity measurements with the scintillation counter. The calibration was absolute, i.e., the voltage signal appearing on the measured total circuit capacitance gave the total electron charge collected. 26.3 eV was taken for the energy required to produce one ion pair in argon. Bias curves were run to establish that the chamber was being operated in the plateau region of the intensity v s voltage characteristic. The argon filling pressure was adjusted so as to absorb 90% of the incident radiation in the active volume of the chamber. The absolute intensity of Scylla x rays transmitted through thin absorber foils as measured with the argon ionization chamber was found to be ten percent larger than that derived from the NaI scintillation detector. The

¹⁸ H. W. Fulbright, in *Handbuch der Physik*, edited by S. Flügge (Springer-Verlag, Berlin, 1958), Vol. 45, Chap. 1.

¹⁹ W. E. Mott and R. B. Sutton, *Handbuch der Physik*, edited by S. Flügge (Springer-Verlag, Berlin, 1958), Vol. 45, Chap. 3.

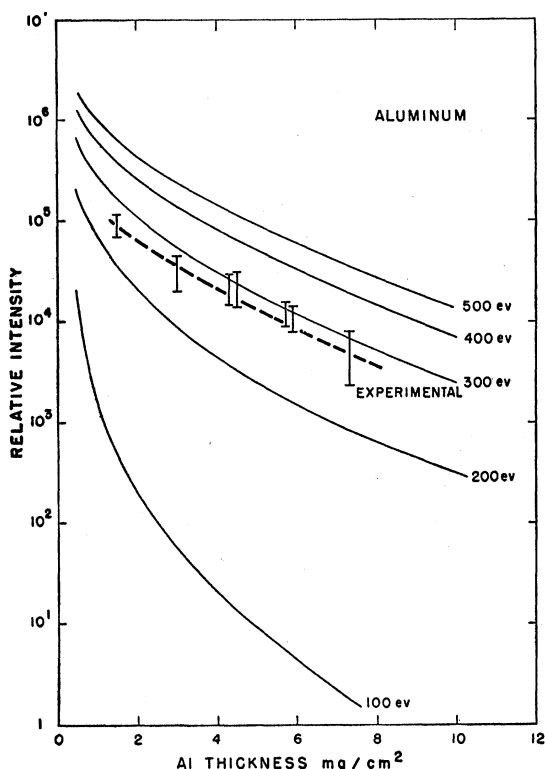


FIG. 8. Experimental aluminum absorption curve compared with calculated transmissions.

difference is not considered significant because the calibrations of the scintillator had already indicated that the absolute value of the sensitivity was subject to at least 20% error. Absorption curves obtained with the ionization chamber were the same shape, within experimental error, as the integrated signal data from both NaI and plastic scintillators, indicating that the response of the scintillators to quanta of 500 ev to 2000 ev energy was sufficiently linear to allow them to be used for this application.

The transmission curves which were obtained for the x rays emitted from Scylla during the second half-cycle of operation are drawn on the same relative scale in Figs. 6 to 9. All exhibit some degree of curvature on a logarithmic plot, indicating that a spectrum of energies is involved, and all indicate x-ray quantum energies of the order of one kev. Each experimental point was established by averaging ten or more separate discharges and the errors indicated are mean deviations from the mean. All data were obtained for operating conditions of 85 kv on the capacitor bank, 90 microns of Hg deuterium pressure, neutron production of a few million per discharge, and a 96% alumina discharge tube. Care was taken to return periodically to a standard absorber thickness throughout any set of observations to ascertain that the x-ray yield of the machine was constant.

Analysis

The self-collision time for particles in a plasma is given by Spitzer²⁰ as:

$$t_c = (11.4A^{1/2}T^{3/2}) / (nZ^4 \ln\Lambda) \text{ seconds,} \quad (5)$$

where T is in degrees Kelvin, n is the number density/cm³, A is the atomic weight and Z the charge state of the colliding particles, and $\ln\Lambda$ is a slowly varying function of n and T , with a value of approximately 10. For electrons this reduces to

$$t_c = (0.26T^{3/2}) / (n_e \ln\Lambda) \text{ seconds.} \quad (5')$$

Over the entire range of the variation of n and T for the Scylla discharge, the electron-electron collision time is sufficiently short compared to the experimental time scale that a Maxwell distribution of electron velocities is expected. In the spectrum analysis, therefore, it is safe to assume that the electrons are at some temperature T_e .

The relative transmission through foils of beryllium, polyethylene, aluminum, and nickel was numerically calculated on an IBM-704 computer for bremsstrahlung spectra, without Gaunt factor corrections, corresponding to electron temperatures of 0.1 to 1.4 kev. The details and the results of these integrations are

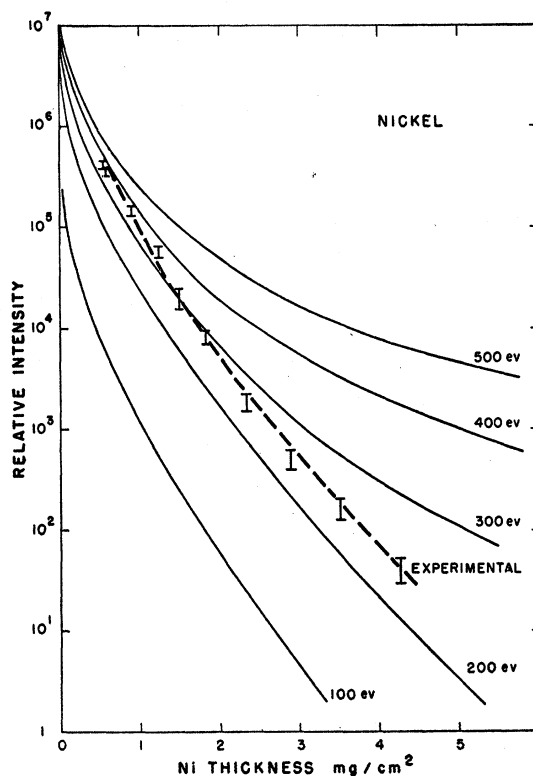


FIG. 9. Experimental nickel absorption curve compared with calculated transmissions.

²⁰ L. Spitzer, *Physics of Fully Ionized Gases* (Interscience Publishers, Inc., New York, 1956).

presented in the Appendix. The experimental transmission data can be compared with these calculations in two ways. First, shapes of the measured absorption curves can be fitted. This type of comparison is shown in Figs. 6 to 9 for the four absorber materials. It is apparent from visual examination that the experimental data fit best an electron temperature between 0.2 and 0.3 kev. The aluminum absorber is not very sensitive to temperatures in this range because the *K* edge at 7.9A makes the mass absorption coefficient from 3A to 8A, nearly the same as it is from 8A to 15A. A second comparison which depends on another property of the absorbers is to compare the relative transmission through foils of different materials so as to take advantage of the selective transmission of aluminum above its *K* edge at 7.9A, of nickel above its *L* edges at 12.5A to 14.6A, and of carbon above its *K* edge at 44.5A. The calculated transmission ratios as a function of temperature can be obtained from the results tabulated in the Appendix for all pairs of absorber materials and thicknesses. Figure 10 shows these calculated ratios for four pairs of materials in the temperature range of 0.1 to 1.0 kev. The experimentally measured ratios are plotted as triangles on the calculated curves. Similar evaluation of a total of twelve ratios

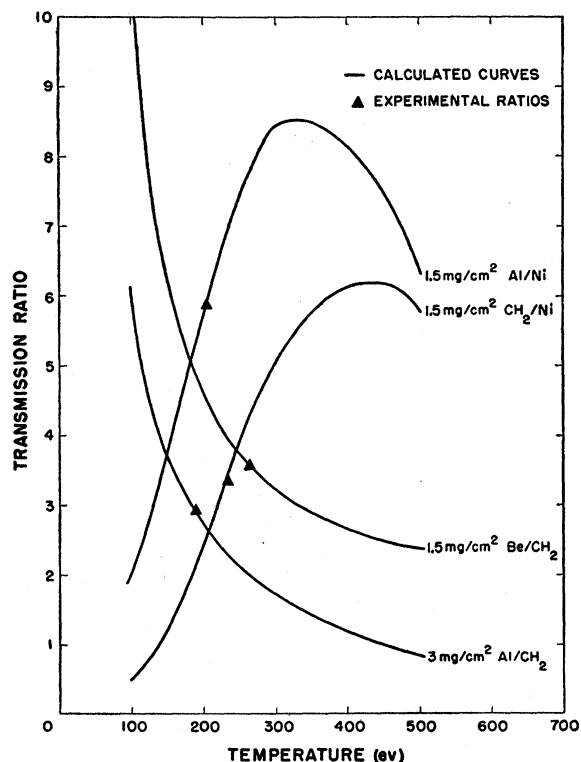


FIG. 10. Ratios of intensities transmitted through different absorber materials of the same mass thickness for bremsstrahlung spectra from different temperature sources. The triangles are the experimentally observed ratios for the appropriate absorbers. Calculations involving CH₂ were corrected for the 100 μg/cm² aluminum film excluding visible light.

TABLE I. Absolute integrated soft x-ray yield in the second half-cycle as determined with three types of detectors. In the third column, the yield is the energy radiated into 4π steradians which is transmitted through 1.46 mg/cm² aluminum.

Detector	Foil (mg/cm ²)	Yield into 4π steradians (joules)
Ion chamber	1.46 Al	(3.5±1)×10 ⁻³
Plastic PM	1.46 Al	(3.2±1)×10 ⁻³
NaI PM	1.46 Al	(3.3±1)×10 ⁻³

averages to 230±40 ev as the best fit of the experimental absorption data to the transmissions expected for deuterium bremsstrahlung. Correction for the free-free Gaunt factor would raise the temperature 13% to 260 ev.

In addition to the indirect methods of inferring the experimental x-ray spectrum described above, it is possible to unfold the absorption curves back to an incident spectrum, within certain bounds. Analytic techniques have proved unsuitable, but a graphical procedure applied to the carbon absorption data allows the experimental curve to be unfolded into a monotonically increasing intensity function from 3A to 12A. 3A corresponds to the highest energy radiation which is appreciably attenuated by the thickest carbon absorber and 12A is the softest radiation which is appreciably transmitted by the thinnest foil. The unfolded spectrum, to an absolute scale, is plotted in the form of log*dE/dν* vs *ν* in Fig. 11. If the radiation spectrum is the result of bremsstrahlung, or of recombination radiation beyond the low-frequency cutoff, the resulting plot will be a straight line of slope $-h/kT$. It should be noted that the solid lines drawn in Fig. 11 correspond to the recombination spectra, for frequencies greater than the low-frequency cutoff, from sources with temperatures of 200 ev, 240 ev, and 280 ev, and have been corrected for the free-bound Gaunt factor.

With the assignment of an electron temperature it is possible to calculate back from the yield to derive a density assuming that the radiating volume has been measured and that the radiation is due to deuterium bremsstrahlung. Three sets of absolute yield determinations integrated over the second half-cycle pulse and corrected for detector sensitivity and solid angle are tabulated in Table I.

Since the temperature and volume determinations are valid only at the time of peak magnetic field, the unintegrated signals from the scintillators must be used for a calculation of the density. The number of watts radiated into 4π steradians at the time of peak magnetic field is tabulated in Table II.

If the emitting region is a prolate spheroid 2-cm long and 1.5-cm diameter, the volume is 2.4 cm³. Substituting in Eq. (3), $T=260$ ev, vol.=2.4 cm³, and $\int_0^\infty (E_\lambda/g)d\lambda=7.6 \times 10^5$ watts, one obtains $N_e N_i=1.3 \times 10^{36}$, or $N_e=N_i=1.1 \times 10^{18}$ cm⁻³. Such a large density, nearly two hundred times greater than the initial deuterium atomic number density, is clearly in

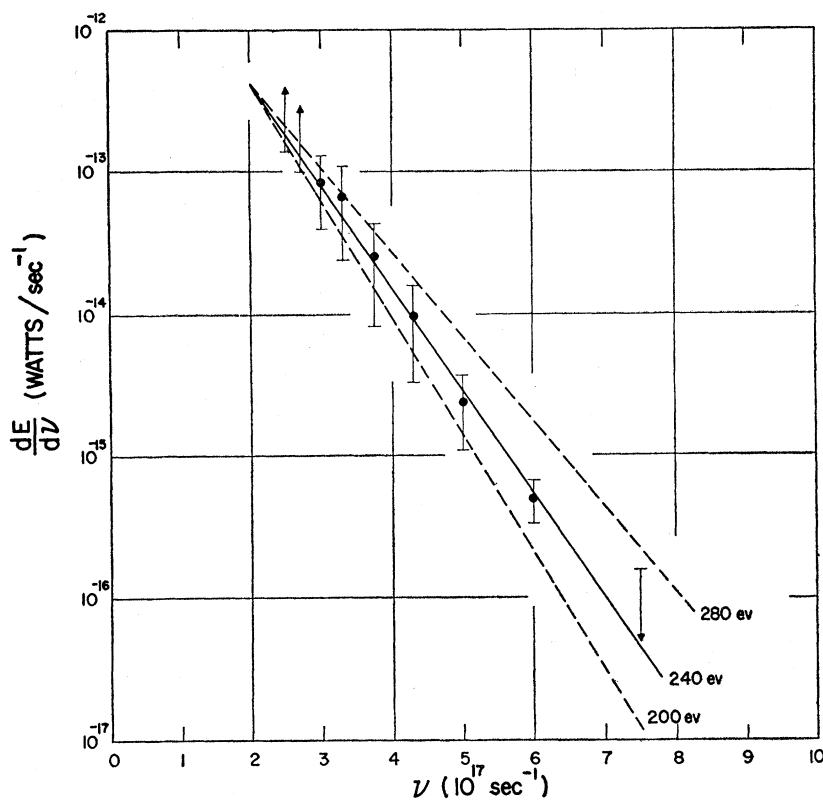


FIG. 11. Scylla radiation spectrum unfolded from the polyethylene absorption data. The straight lines are theoretical slopes for Maxwellian electron velocity distributions at 200 ev, 240 ev, and 280 ev temperatures.

disagreement with the ion and electron densities derived by techniques involving the geometrical compression and the absolute intensity of the visible continuum. From the point of view of the radiation intensity, the power radiated in the soft x-ray region is 260 times greater than pure deuterium bremsstrahlung at the temperature and density determined from other information. Therefore radiation processes in addition to pure bremsstrahlung are indicated.

The presence of high- Z impurity atoms is the most likely cause of the large radiated power. In addition to increasing the free-free radiation because of the Z^2 dependence of the radiation intensity, impurities give rise to recombination and line radiation. Beyond the low-frequency cutoff, the intensity of recombination

radiation has the same frequency distribution as the free-free radiation, but the absolute intensity is very much greater than the free-free radiation because of the discrete final state. Line radiation has even greater total integrated intensity than recombination radiation but because it involves transitions between bound states, the frequency of the emitted lines is necessarily less than recombination radiation arising from free electrons falling to the ground state of the particular ion species. Because of these properties, a valid temperature determination is possible even in the presence of impurity ions and line radiation if the continuum at the high-frequency limit of the spectrum is identified. A slight adjustment of the interpretation of the spectrum in terms of a temperature is necessary because of the different Gaunt correction for recombination radiation.

Two experiments were performed to substantiate the assumption of impurity atoms as the source of the high-frequency limit continuum. First, line radiation from likely impurity materials was surveyed with a photoelectric recording vacuum-ultraviolet monochromator. Of the most probable impurities, carbon from the oil diffusion pumps, oxygen and nitrogen from air contaminant, and oxygen and aluminum from the ninety-six percent alumina discharge tube, only oxygen was detected at the center of the discharge during the second half-cycle of current. Spectra of low ionization states of oxygen appeared just after the

TABLE II. Absolute soft x-ray intensity at the peak compression of the second half-cycle. The fourth column is the extrapolation factor to zero absorber thickness, assuming that the spectrum is the result of bremsstrahlung from a deuterium plasma at an electron temperature of 260 ev.

Absorber	Thickness (mg/cm ²)	Yield into 4 π steradians (watts)	Extrapolation to zero absorber	Total yield into 4 π steradians (watts)
Al	1.46	4.4×10^8	158	6.9×10^8
CH ₂	1.03	5.4×10^8	145	7.9×10^8
Be	1.45	9.8×10^8	79	7.7×10^8
Ni	0.55	19.4×10^8	40	7.8×10^8

peak of the current and then increased steadily in intensity until the end of the half-cycle. O^{VI} appeared just before the second half-cycle current peak, decreased to a low level at the current maximum, and then rose to a high level with the current decay. Such behavior suggests that the population of the O^{VI} species was depleted as the impurity atoms were more completely stripped by the increasing electron temperature, and after the maximum electron temperature was passed with the peak magnetic field, O^{VI} was repopulated. A heretofore unobserved triplet in the helium-like spectrum of O^{VII} corresponding to the $2s\ ^3S-2p\ ^3P$ transitions²¹ was identified, confirming the existence of very highly ionized oxygen species. The presence of the O^{VII} triplet is itself a valuable confirmation of the high electron temperature because the final state of the transition lies 561 eV above the ground state of O^{VII} . Oscillograph records of the time history of lines of O^{IV} to O^{VII} are shown in Fig. 12. The increase of intensities with the third and subsequent half-cycles is typical and reflects the growth of impurities in the discharge.

As the second test for the presence of impurity in the

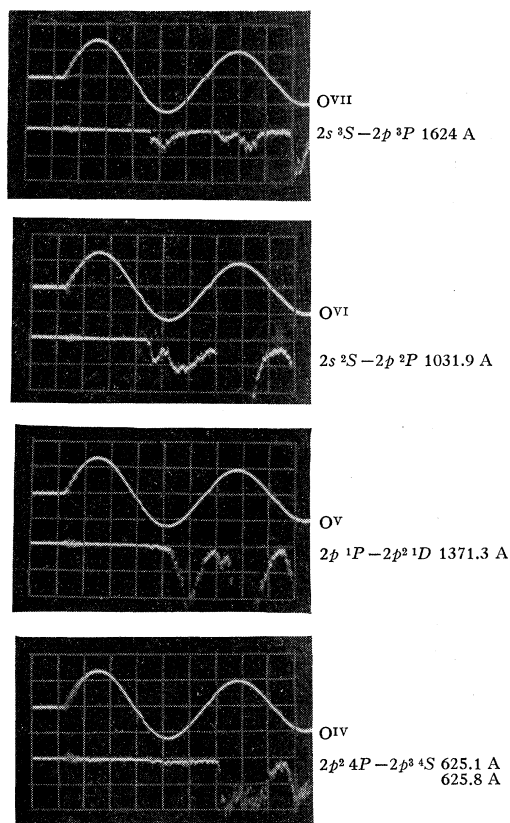


FIG. 12. Time resolved spectra of oxygen impurity. One large division of the oscilloscope grid is $1\ \mu\text{sec}$. The top trace of each photograph is the driving magnetic field. The highest electron temperature occurs at the maximum of the second half-cycle.

²¹ B. Edlen, Arkiv Fysik 4, 441 (1952).

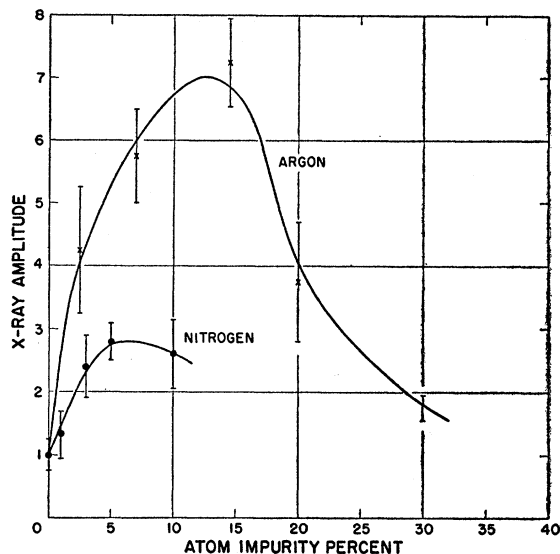


FIG. 13. X-ray amplitude transmitted through $1.5\ \text{mg}/\text{cm}^2$ aluminum absorber as a function of added impurities. The amplitude is normalized to unity in the absence of added impurity.

discharge, known fractions of nitrogen, neon, and argon were added to the deuterium filling. For example, the addition of about one percent of argon to a pure deuterium discharge is expected to give rise to recombination radiation of several hundred times greater intensity than the deuterium x-ray bremsstrahlung, and should reduce the electron temperature considerably. The actual change of x-ray intensity for nitrogen and argon contaminants is shown in Fig. 13 where it is seen that only factors of two or so were the actual increases. In addition, absorption measurements taken for both five percent nitrogen and five percent argon showed that the high frequency cutoff shifted to longer wavelengths by only about ten percent, so that the electron temperature was still in excess of 200 eV.

These experiments provide strong evidence that the Scylla discharge is contaminated by the order of two percent impurity, and that the impurity is mainly oxygen. The soft x rays are then mainly due to recombination radiation from highly ionized oxygen atoms instead of free-free bremsstrahlung from deuterium, and the temperature must be corrected by about three percent from 230 eV (the best fit to the classical bremsstrahlung spectrum) to 240 ± 40 eV to allow for the free-bound Gaunt factor. Corrections for the low-frequency limit of recombination radiation are unimportant because the absorbers have already filtered the spectrum so that the longer wavelength portion of the bremsstrahlung spectrum makes a negligible contribution to the transmitted energy.

In order to calculate the spectral shape and intensity from an oxygen contaminated deuterium discharge for comparison with the observed spectrum, it is necessary to first estimate the populations of the oxygen ion

TABLE III. Ionic populations and radiation intensities from oxygen contaminant in a deuterium plasma at an electron temperature of 240 ev. χ_n and λ_i are the ionization energy and corresponding cutoff wavelength of each oxygen ion species. The populations are derived from Eq. (6). The fifth column is the ratio, per atom, of recombination radiation from oxygen ions to deuterium bremsstrahlung. The last two columns are the ratio of oxygen bremsstrahlung to deuterium bremsstrahlung and the ratio of the total radiation intensity, for $\lambda < \lambda_i$, to deuterium bremsstrahlung, for each ion component, assuming 2% oxygen contaminant in the discharge.

Species	χ_n ev	λ_i ang- stroms	Relative popula- tion	$(f-b)O$		
				$E_\lambda(f-f)D$ (per atom)	$E_\lambda(f-f)O$ (2% oxygen)	$E_\lambda(f-f)D$ (2% oxygen)
O ^{VI}	138.1	89.8	0.00004	22	0.00002	0.00004
O ^{VII}	739.1	16.8	0.09	41	0.065	0.14
O ^{VIII}	871.1	14.2	0.47	3620	0.46	34.
O ^{IX}	0.44	17500	0.56	155.

species and then calculate the spectrum and intensity from each ion species.

Elwert^{22,23} gives an equation for the calculation of the relative population of the i th and $i+1$ th ionized states for a case where equilibrium is obtained through collisional excitation and photo-recombination (photo-ionization and three-body collisional recombination negligible). It is:

$$\frac{N_{i+1}}{N_i} = \frac{3\sqrt{3} f_2 \xi_{n_0} (\chi_H)^2 e^{-\chi_{n_0}/kT_e}}{16\alpha^3 f_1 g n_0 (\chi_{n_0}) \chi_{n_0}/kT_e} \quad (6)$$

χ_{n_0} is the ionization energy of the ground shell of total quantum number n_0 , χ_H is the hydrogen ionization potential, ξ_{n_0} is the number of electrons in the n_0 th shell, α is the fine structure constant, g is a factor of order 2 to account for recombinations into higher shells, and f_1 and f_2 are quantum mechanical correction factors of value $f_2/f_1 \approx 1.25$. The multiplier $(3^3 f_2)/(16\alpha^3 f_1 g)$ is, to good approximation, 5×10^5 . If one assumes that oxygen impurity ionic populations are governed by Eq. (6),²⁴ and that the total oxygen impurity is two percent, the results of Table III apply for an electron temperature of 240 ev. The values of the ionization potentials are taken from Allen.²⁵

From this table it is clear that the calculated radiation intensity below the 14.2A recombination spectrum limit for two percent oxygen impurity is in good agreement with the observed yield, especially when it is recognized that no account has been taken of radiation arising from n values greater than the ground state.

²² G. Elwert, Z. Naturforsch. 7a, 432 (1952).

²³ G. Elwert, Z. Astrophysik 41, 67 (1956).

²⁴ The early and symmetric appearance of the O^{VII} radiation is experimental support for this assumption. The calculated collision ionization cross sections of Knorr¹⁹ imply that it is marginal whether steady state concentrations have been reached with the Scylla experimental conditions.

²⁵ C. W. Allen, *Astrophysical Quantities* (The Athlone Press, London, 1955).

The effect of these shells is typically to increase the intensity 15 or 20%.

For regions of the spectrum where the wavelength is longer than the recombination limit, and which are free of emission lines, 2% oxygen at the assumed temperature, adds 109% to the deuterium free-free bremsstrahlung, in addition to increasing the electron density 15% over the deuterium ion density.

Figure 14 shows a reconstruction of the general features of the spectrum of radiation anticipated from a deuterium discharge contaminated with 2% oxygen, at an electron temperature of 240 ev. In addition to the continua, some of the resonance line radiation is indicated, with intensities taken from Elwert¹⁹ who estimated the matrix elements for application to the solar corona at $T=260$ ev. The resonance lines from O^{VIII} and O^{VII} are at sufficiently long wavelengths to require no correction to the temperature assignment from the absorption data.

IV. VISIBLE LIGHT MEASUREMENTS

Experimental Apparatus

The Scylla discharge was viewed axially with the coil center imaged (demagnified approximately 20%) on the 400 micron wide, one mm high slit of a grating spectrograph. Six photomultiplier detectors utilized

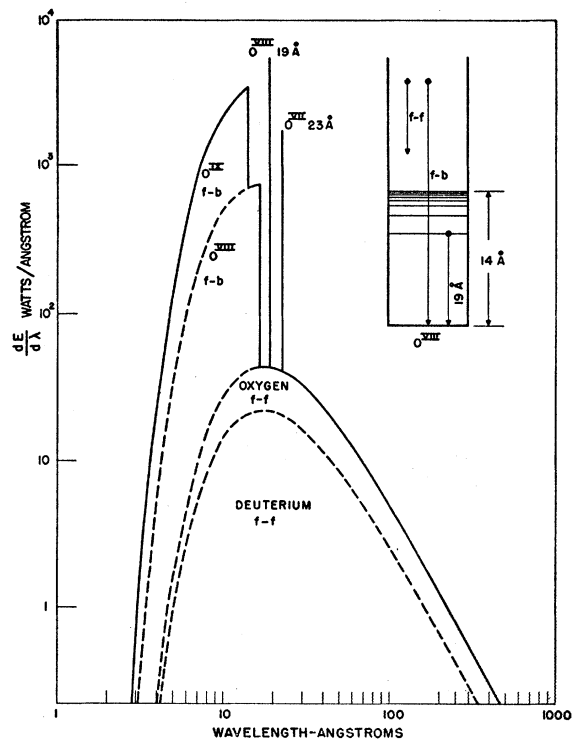


Fig. 14. Composition of the radiation spectrum of Scylla. An examination of the spectral shape and absolute intensity below the free-bound limits and in the visible, together with a search for contaminant spectral lines, is sufficient to determine the electron temperature and density, and percentage and nature of contaminating materials.

subsidiary optics to view 150 micron wide slits in the film plane of the 11A/mm dispersion instrument. Three 6328 photomultipliers set for wavelengths between 4000 and 6500 angstroms, each with a Corning filter No. 3389 to eliminate the second order of lower wavelengths, and three 1P28 photomultipliers set for wavelengths between 3500 and 4000 angstroms covered the visible spectrum. The 1P28 tubes observed in the second order (higher grating efficiency) and a Corning filter No. 4305 eliminated the first order spectrum. The wavelength separation of the detectors was fixed and wavelength changes were made common to all units by rotating the grating. Wavelength calibrations were made with the 5460A line of mercury.

The output signal cables, shielded with copper pipe, were led to oscilloscopes inside a shielded room in order to reduce pickup from the main capacitor discharge. The low signal levels made it necessary to reduce noise levels with low-pass sharp cutoff (≈ 3 Mc/sec) electrical filters at the cable terminations. Two four-beam oscilloscopes²⁶ displayed the six signals, with one beam on each oscilloscope recording the magnetic field. In addition, a dual-beam oscilloscope displayed the magnetic field and the soft x rays monitored by a scintillator-photomultiplier detector in fixed geometry within the Scylla tube. This monitor provided time correlation with the soft x rays in the data reduction. The oscilloscope deflections were calibrated with single pulse square waves of known voltage from a Hewlett-Packard 212A pulser with fixed attenuation steps.

The optical alignment was accomplished with the aid of a point light source at the object point. Two separate alignments were made during the course of the experiment—once on the geometrical center of the coil and once displaced two mm toward the electrical feedpoint. No differences were observed in the spectrum, in agreement with the fact that a 1.5-cm diameter hot core is seen on the soft x-ray photographs.

Absolute intensity calibrations were made with a tungsten ribbon filament operated at controlled brightness temperature placed at the source position. The true temperature and the spectral intensity distribution were computed with the emissivity data of DeVos.²⁷ The dc output level of the detectors was adjusted during calibration with a wavelength-calibrated neutral density filter to give an adequate signal-to-noise ratio while still being well within the region of linear response.

The largest error in the calibration was an uncertainty in the correction factor for the transmission of the Pyrex end window of the discharge tube. The window transmission changed after every discharge because of deposits of impurities driven from the tube walls. In order to minimize this correction, the end window was always protected by a flap valve except during dis-

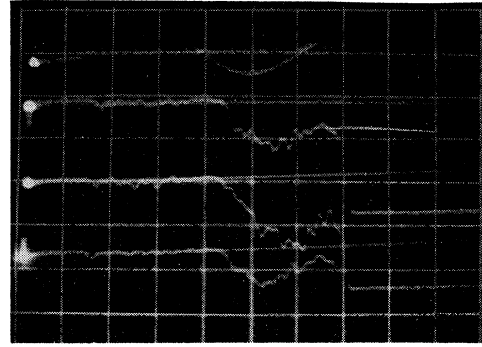


FIG. 15. Four-beam oscilloscope traces of magnetic field (top trace) and photomultiplier signals for three different wavelengths. One large division of the oscilloscope grid is $1 \mu\text{sec}$. Light signals were read just before the peak of the second half-cycle; saturation in the third half-cycle is due to impurities.

charges when data were taken, and was replaced after a maximum of fifteen discharges. At the end of the experiment the transmission of each window was measured as a function of wavelength and proportional corrections were applied to the data, with the assumption that the total transmission loss was the result of equal decrements for each discharge. The largest correction was 30%.

The primary uncertainty in the experiment was due to the lack of a clearly defined peak signal at the time of interest. The signals usually showed a short plateau in a rising signal which was partly obscured by the noise characteristic of the photomultipliers in the presence of a signal. One example of a four-beam oscilloscope trace is shown in Fig. 15. The period of the magnetic field (top trace) is $5 \mu\text{sec}$ and neutrons and x rays were produced for about one μsec near the peak of the second half-cycle. Failure to observe a decrease of the light signal after peak magnetic compression was the result of competition between decompression of the plasma, producing decreased intensity, lower temperature, producing increased intensity, and arrival of impurities, producing greatly increased intensity. The situation is further complicated by the possibility of varying intensity contributions from the large tube region through which the core is viewed. The very large rise in light intensity seen at the end of the second half-cycle in Fig. 15, appeared $1.2 \mu\text{sec}$ earlier when the discharge was viewed one cm off center, indicating that this was an impurity influx from the wall. The same impurity influx from the walls was observed in streak camera pictures.⁴

Analysis

In analyzing the visible light data, the six channels were read at the time corresponding to the x-ray peak, and the maximum and minimum within $0.2 \mu\text{sec}$ of this time recorded to give a range of the uncertainty. Figure 16 shows the data obtained from two discharges of Scylla. The intensity recorded in each of the channels

²⁶ J. Winston, Los Alamos Scientific Laboratory Report LA-2281 (unpublished).

²⁷ J. C. DeVos, *Physica* 20, 690 (1954).

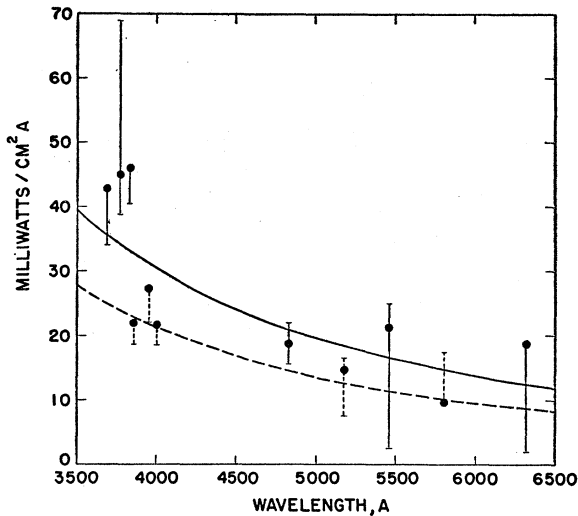


FIG. 16. Brightness vs wavelength for two separate discharges. The solid and dotted lines are best λ^{-2} fits. The difference is typical of the variation between discharges.

is plotted with the possible range assigned to each point. The central dot is the value obtained at the presumed correct time from the x-ray monitor. Through each set is fitted a theoretical λ^{-2} curve [Eq. (2)]. That these curves differ in absolute value reflects the difference in conditions between separate discharges. The points near the Balmer discontinuity which fall above one of the curves are typical and are due to line emission and free-bound emission in cooler outer layers of the discharge. Of sixteen discharges analyzed in this manner, only two could not be fitted with a λ^{-2} curve when neglecting the one or two points near the Balmer discontinuity. While the ranges of uncertainty are so large and the wavelength spread covered is so small that these data cannot be regarded as proof of a λ^{-2} behavior, the data are consistent with the expected bremsstrahlung spectral shape.

The averages at the various wavelengths covered by the sixteen discharges are shown in Fig. 17. The ordinate is in units of measured brightness, i.e., it must still be divided by an optical depth before being compared with Eq. (2). The solid bars are the root mean square errors of the central dots, and the broken bars are independent averages for the maximum and minimum signal values within the 0.2 μ sec interval discussed above. The small numbers indicate the number of data points contributing at each wavelength. The λ^{-2} curve has been drawn to represent an average of the points above 4500 Å. The fact that three points below 4500 Å fall below this line is primarily a consequence of the fact that these happen to be averages of just two discharges, both of low absolute value. Neither the high intensity of D_{β} (4860 Å), nor the shift in the Balmer discontinuity (the result of the merging of the upper discrete levels through Stark broadening), are consistent with the core temperature derived from the

soft x rays or the core density derived from the visible continuum. They are, however, readily explained by assuming their origin is in a cooler, less dense, outer layer of the discharge.

In contrast to the x-ray intensity, the visible continuum is in fair agreement with pure deuterium bremsstrahlung. Because of the strong dependence of the free-bound spectrum on the ionization potential and the principal quantum number of the final state, and because of the small population of lowly ionized atoms at the center of the discharge, recombination radiation is not an important contribution to the continuum for quantum energies much less than kT_e .

The light intensity obtained from Fig. 17, together with the electron temperature of 240 eV obtained from the x-ray measurements and an optical depth of the hot plasma of two cm obtained from the neutron collimation measurements provide sufficient data so that Eq. (2) can be solved for the electron density. With a Gaunt factor $\bar{g}=3$ at 5000 Å, the electron density is found to be $(7\pm 1)\times 10^{16}/\text{cm}^3$ before correction for the oxygen impurity. If two percent oxygen contaminated the fireball, Table III shows that the highly ionized states of oxygen contributed as much to the visible continuum as did the deuterium, so that the electron density was $5\pm 1\times 10^{16}/\text{cm}^3$. In addition, 15% of the electrons came from the oxygen so that the deuterium density was about $4.3\times 10^{16}/\text{cm}^3$, corresponding to a magnetic compression of about eight, in agreement with observations of the size of the soft x-ray and neutron emitting region.

The first half-cycle of the discharge when there are no neutrons or soft x rays showed prominent D_{β} radiation on the axis of the discharge. The observed intensity indicated that the electron temperature was less than 10 eV at that time. The density in the first half-cycle derived from a modified Holtsmark distribution²⁸ applied to the observed line broadening was about half that in the second half-cycle.

V. DISCUSSION

The experiments herein reported show that techniques are available for the diagnosis of extremely high-temperature plasmas. In review, by an analysis of the continuum radiation from Scylla, the maximum electron temperature and density have been established, as well as the state of the discharge with respect to impurity ions. In addition, the deuteron density was inferred from the measured electron density by a suitable correction for the impurity ions.

Although the exact heating mechanism of the discharge has not been conclusively established, these results are in agreement with the proposal that a strong hydromagnetic shock serves as the preheater before the adiabatic compression of the plasma by

²⁸ M. Lewis and H. Margenau, Revs. Modern Phys. **31**, 569 (1959).

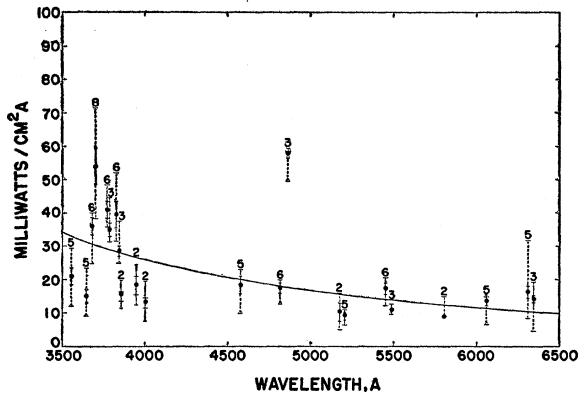


FIG. 17. Brightness vs wavelength—composite results for sixteen discharges fitted to a λ^{-2} curve. The high value at 4860 Å is D_{β} line radiation. The numbers indicate how many data points contribute at each wavelength.

the rising magnetic mirror field.^{1,4} In particular, since the peak electron temperature is only about one-fifth of the deuteron temperature at the same time, the shock preheater is particularly attractive as a mechanism to provide greater energy to the ions than to the electrons, as opposed for example, to a process involving joule heating before the adiabatic compression. Because of the density and time scale of the Scylla experiment, equipartition of energy between light and heavy particles cannot have taken place, so that a difference in the ion and electron temperatures reflecting the initial heating mechanism should be observed. The electron energy loss by radiation is not large enough to invalidate the argument that the electron temperature reflects the preheater mechanism. Spitzer²⁰ gives the equipartition time between groups of particles of mass numbers A and A_1 , at temperatures T and T_1 °K, and density n/cm^3 :

$$t_{eq} = \frac{5.87 A A_1}{n Z^2 Z_1^2 \ln \Lambda} \left(\frac{T}{A} + \frac{T_1}{A_1} \right)^{3/2} \text{ seconds,} \quad (7)$$

where $\ln \Lambda$ is the same factor of order ten appearing in Eq. (5). For the discharge temperatures and densities, the electron-electron thermalizing time is the order of 10^{-9} second; the deuteron-deuteron thermalizing time is the order of 10^{-6} second; and the electron-deuteron thermalizing time is the order of 5×10^{-6} second. The individual particle groups therefore have Maxwellian velocity distributions but different temperatures.

The oxygen impurity may be a basic contaminant of most high power deuterium discharges. In this particular experiment, the discharge tube wall material is 96% Al_2O_3 , and spectral evidence indicates that although oxygen is present early, aluminum is not. This suggests that the oxygen is not from the alumina directly, but perhaps comes from D_2O formed as the discharge dies out and absorbed on the wall after each shot. A monatomic layer of D_2O released from the wall would produce about ten times as much oxygen per

unit length as is observed. More careful spectroscopic studies should resolve the question of the source of the early oxygen contaminant.

The presence of oxygen impurity in the discharge increases the radiated energy loss by a large factor over the uncontaminated deuterium bremsstrahlung loss. Knorr¹² calculates that at 240-ev the free-bound radiation from oxygen exceeds the free-free oxygen radiation by a factor 6, and the bound-bound radiation exceeds the free-free radiation by a factor 25. In all, then, since Table III shows that the free-free radiation from the oxygen is about equal to the free-free radiation from the deuterium, the total radiated energy loss is about 30 times greater than bremsstrahlung from an uncontaminated deuterium plasma at the same temperature. The plasma therefore radiates a total of about 7×10^4 watts at the time of peak compression.

In addition to the value of the Scylla experiment as an approach to controlled thermonuclear research, its application as a source of radiating plasma at a temperature near that of the solar corona should lead to fundamental results of interest to the study of stellar surfaces. Not only can equilibrium processes be examined, but nonstationary systems can be studied for the measurement of excitation and ionization cross sections which are poorly known.

VI. ACKNOWLEDGMENTS

It is a pleasure to recall many essential discussions with Drs. K. Boyer, F. L. Ribe, and J. L. Tuck and with Dr. R. S. Pease of Atomic Energy Research Establishment, Harwell. In addition, the services of D. C. Camp, W. D. Gould, L. H. McDowell, and V. L. Stewart greatly facilitated the experimental work; Dr. J. D. Thomas and Mrs. N. B. Browne performed the major portion of the IBM-704 calculations. The assistance of other persons of the laboratory has been mentioned in the text and is gratefully acknowledged.

APPENDIX

The transmission of thin films of beryllium, CH_2 (polyethylene), aluminum, and nickel has been calculated for classical bremsstrahlung spectra in the temperature range of 0.1 to 1.4 kev. The absorption characteristics of these materials are such that the entire transmission occurs in the range of wavelengths of 1 to 100 angstroms. The quantum-mechanical (Gaunt) correction is neglected in the calculations of relative transmission in the belief that calculations without the correction will in general be more useful. Neglecting the Gaunt factor results in a temperature estimate about ten percent low if these calculations are applied to a free-free spectrum and an estimate about three percent low for a free-bound spectrum.

Polyethylene is transparent to visible radiation, and some precaution must be taken to assure that visible wavelengths are not transmitted.

TABLE IV. Fraction of total intensity transmitted through absorber foils—classical bremsstrahlung spectrum.^a

Absorber	Thickness mg/cm ²	T_e	100 ev	200 ev	300 ev	400 ev	500 ev	600 ev	800 ev	1000 ev	1200 ev	1400 ev
CH ₂	0		1	1	1	1	1	1	1	1	1	1
	0.5		2.02(-2)	4.27(-2)	7.14(-2)	1.08(-1)	1.52(-1)	1.69(-1)	2.53(-1)	3.25(-1)	3.90(-1)	4.41(-1)
	1.0		4.04(-3)	1.06(-2)	2.56(-2)	5.03(-2)	8.20(-2)	1.11(-1)	1.81(-1)	2.47(-1)	3.09(-1)	3.60(-1)
	1.5		9.98(-4)	3.61(-3)	1.30(-2)	3.10(-2)	5.61(-2)					
	3		2.38(-5)	4.97(-4)	4.12(-3)	1.32(-2)	2.80(-2)	4.69(-2)	9.23(-2)	1.41(-1)	1.90(-1)	2.36(-1)
	5		3.91(-7)	1.38(-4)	1.70(-3)	6.60(-3)	1.57(-2)	2.85(-2)	6.21(-2)	1.02(-1)	1.44(-1)	1.85(-1)
	7							1.97(-2)	4.64(-2)	7.98(-2)	1.17(-1)	1.54(-1)
	9		1.21(-8)	2.80(-5)	5.37(-4)	2.63(-3)	7.27(-3)	1.46(-2)				
	11			1.54(-5)		1.85(-3)		1.14(-2)	3.00(-2)	5.55(-2)	8.56(-2)	1.17(-1)
	13			9.16(-6)	2.37(-4)	1.37(-3)	4.21(-3)	9.10(-3)				
	15			5.71(-6)	1.68(-4)	1.04(-3)	3.35(-3)	7.54(-3)				
	20			2.12(-6)	8.18(-5)	5.85(-4)	2.07(-3)	4.93(-3)				
	30			4.59(-7)	2.67(-5)	2.39(-4)	9.75(-4)	2.75(-3)				
	50			5.24(-8)	5.47(-6)	6.73(-5)	3.36(-4)	1.02(-3)				
	Be	0		1	1	1	1	1	1	1	1	1
0.5			2.13(-3)	3.21(-2)	8.88(-2)	1.51(-1)	2.15(-1)	2.70(-1)				
1.0			5.44(-4)	1.47(-2)	5.07(-2)	9.73(-2)	1.48(-1)	1.97(-1)	2.85(-1)	3.59(-1)	4.24(-1)	4.76(-1)
1.5			3.53(-4)	8.63(-3)	3.46(-2)	7.19(-2)	1.16(-1)	1.59(-1)				
3			3.55(-5)	3.02(-3)	1.62(-2)	3.95(-2)	7.02(-2)	1.04(-1)	1.72(-1)	2.37(-1)	2.97(-1)	3.49(-1)
5			7.47(-6)	1.22(-3)	8.43(-3)	2.35(-2)	4.56(-2)	7.14(-2)	1.28(-1)	1.86(-1)	2.41(-1)	2.91(-1)
7			2.38(-6)	6.28(-4)	5.19(-3)	1.60(-2)	3.30(-2)	5.42(-2)	1.03(-1)	1.55(-1)	2.07(-1)	2.54(-1)
9			9.45(-7)	3.68(-4)	3.52(-3)	1.17(-2)	2.55(-2)	4.34(-2)	8.65(-2)	1.34(-1)	1.82(-1)	2.28(-1)
11				2.33(-4)		9.05(-3)		3.59(-2)	7.48(-2)	1.18(-1)	1.64(-1)	2.07(-1)
15			1.19(-7)	1.10(-4)	1.46(-3)	5.85(-3)	1.43(-2)	2.62(-2)				
Al	0		1	1	1	1	1	1	1	1	1	1
	0.5		3.00(-3)	2.77(-2)	7.09(-2)	1.15(-1)	1.57(-1)	1.81(-1)	2.38(-1)	2.87(-1)	3.30(-1)	
	1.0		3.20(-4)	8.72(-3)	3.05(-2)	5.66(-2)	8.28(-2)	1.04(-1)	1.43(-1)	1.77(-1)	2.10(-1)	2.40(-1)
	1.5		8.53(-5)	4.36(-3)	1.79(-2)	3.52(-2)	5.29(-2)	6.83(-2)				
	3		9.38(-6)	1.17(-3)	5.98(-3)	1.29(-2)	2.02(-2)	2.70(-2)	3.99(-2)	5.36(-2)	6.97(-2)	8.67(-2)
	5		1.57(-6)	3.47(-4)	2.04(-3)	4.69(-3)	7.61(-3)	1.04(-2)	1.63(-2)	2.35(-2)	3.31(-2)	4.46(-2)
	7		4.13(-7)	1.30(-4)	8.36(-4)	1.98(-3)	3.28(-3)	4.57(-3)	7.55(-3)	1.20(-2)	1.85(-2)	2.69(-2)
	9		1.36(-7)	5.44(-5)	3.71(-4)	9.01(-4)	1.52(-3)	2.16(-3)	3.85(-3)	6.76(-3)	1.15(-2)	1.81(-2)
	11			2.45(-5)		4.29(-4)		1.07(-3)	2.09(-3)	4.13(-3)	7.71(-3)	1.30(-2)
	15		9.35(-9)	5.61(-6)	4.20(-5)	1.06(-4)	1.88(-4)	2.92(-4)				
Ni	0		1	1	1	1	1	1	1	1	1	1
	0.5		1.42(-3)	1.57(-2)	3.50(-2)	5.34(-2)	7.31(-2)	9.33(-2)	1.35(-1)	1.78(-1)	2.22(-1)	2.61(-1)
	1.0		2.49(-4)	3.08(-3)	7.61(-3)	1.31(-2)	2.08(-2)	3.05(-2)	5.57(-2)	8.61(-2)	1.20(-1)	1.53(-1)
	1.5		4.35(-5)	7.79(-4)	2.13(-3)	4.35(-3)	8.28(-3)	1.40(-2)	3.11(-2)	5.38(-2)	8.03(-2)	1.08(-1)
	3		8.98(-7)	2.19(-5)	1.08(-4)	4.75(-4)	1.49(-3)	3.46(-3)	1.08(-2)	2.27(-2)	3.82(-2)	5.61(-2)
	5		1.01(-8)	4.30(-7)	1.08(-5)	9.46(-5)	4.11(-4)	1.14(-3)	4.50(-3)	1.08(-2)	2.01(-2)	3.16(-2)
	7		1.52(-10)	3.25(-8)	2.59(-6)	3.14(-5)	1.61(-4)	5.07(-4)	2.35(-3)	6.30(-3)	1.25(-2)	2.05(-2)

^a The number in parentheses is the power-of-ten multiplier of the transmission.

The absorption coefficients have been obtained from the literature and the K and L edges have been included in the transmission calculations. Where Victoreen's empirical formulas²⁹ are applicable, the IBM 704 has calculated the absorption coefficient; just below the L edge and at all longer wavelengths, the tabulated experimental absorption coefficients of Gilmore³⁰ are interpolated by the 704.

The transmitted intensity is the result of numerically

²⁹ J. A. Victoreen, J. Appl. Phys. **20**, 1141 (1949).

³⁰ F. R. Gilmore, preliminary version, The Rand Corporation Report RM-2367-AEC, 1959 (unpublished).

integrating in 0.1 A intervals the product of the bremsstrahlung spectrum and the exponential absorption factor, with normalization to unity at zero absorber. The results of these calculations are presented in tabular form in Table IV, and are expressed as the fraction of the total energy transmitted through the absorber foil. From these calculations, it is possible to prepare absorption curves for a given material and electron temperature and also the ratios of the transmission through foils of different materials and thicknesses as a function of temperature. The number in parentheses is the power-of-ten multiplier of the transmission.

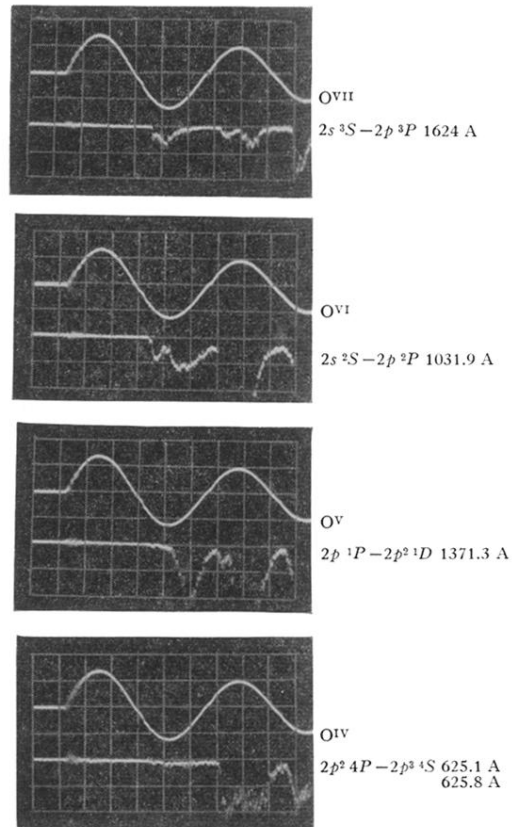


FIG. 12. Time resolved spectra of oxygen impurity. One large division of the oscilloscope grid is $1\ \mu\text{sec}$. The top trace of each photograph is the driving magnetic field. The highest electron temperature occurs at the maximum of the second half-cycle.

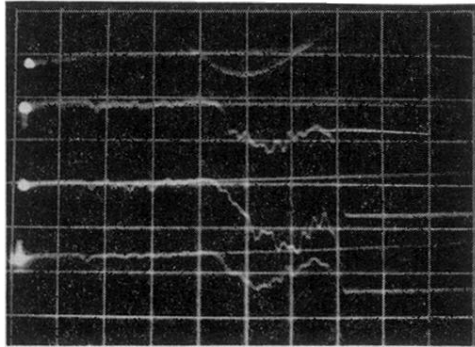


FIG. 15. Four-beam oscilloscope traces of magnetic field (top trace) and photomultiplier signals for three different wavelengths. One large division of the oscilloscope grid is $1 \mu\text{sec}$. Light signals were read just before the peak of the second half-cycle; saturation in the third half-cycle is due to impurities.

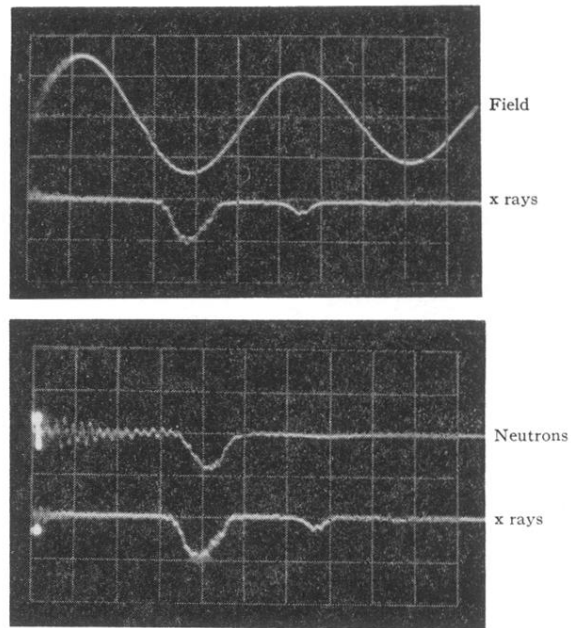


FIG. 3. X-ray and neutron correlation with the driving magnetic field. One large division of the oscilloscope grid is 1 μ sec. The two oscillograms were recorded for the same discharge.

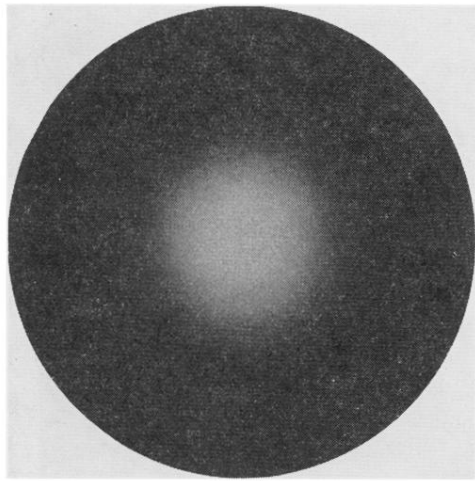


FIG. 4. Pinhole photograph of soft x rays emitted along the discharge tube axis. The circular boundary corresponds to the 5.1-cm inside diameter of the discharge tube at the mid-plane of the driving coil.